CHIN. PHYS. LETT. Vol. 34, No. 8 (2017) 084301

Cavitation Bubble Collapse near a Curved Wall by the Multiple-Relaxation-Time Shan–Chen Lattice Boltzmann Model *

Hong-Hui Xue(薛洪惠)[1], Feng Shan(单锋)[1], Xia-Sheng Guo(郭霞生)[1], Juan Tu(屠娟)[1], Dong Zhang(章东)[1,2]**

[1]*Key Laboratory of Modern Acoustics (MOE), School of Physics, Collaborative Innovation Center of Advanced Microstructure, Nanjing University, Nanjing 210093*

[2]*State Key Laboratory of Acoustics, Chinese Academy of Science, Beijing 100190*

(Received 18 April 2017)

The cavitation bubble collapse near a cell can cause damage to the cell wall. This effect has received increasing attention in biomedical supersonics. Based on the lattice Boltzmann method, a multiple-relaxation-time Shan–Chen model is built to study the cavitation bubble collapse. Using this model, the cavitation phenomena induced by density perturbation are simulated to obtain the coexistence densities at certain temperature and to demonstrate the Young–Laplace equation. Then, the cavitation bubble collapse near a curved rigid wall and the consequent high-speed jet towards the wall are simulated. Moreover, the influences of initial pressure difference and bubble-wall distance on the cavitation bubble collapse are investigated.

PACS: 43.25.+y, 43.80.+p DOI: 10.1088/0256-307X/34/8/084301

The cavitation bubble collapse in liquid near a cell has a destructive effect on the wall due to the resulting high-speed jet.[1] Miller *et al.* reviewed the vitro bio-effects of inertial ultrasonic cavitation from a mechanistic perspective.[2] Carstense *et al.* investigated the in vivo bio-effects generated by the acoustic cavitation.[3] Salgaonkar *et al.* presented the passive cavitation imaging with ultrasound arrays potential application in real-time monitoring of ultrasound ablation.[4] Yoshizawa *et al.* reviewed the high intensity focused ultrasound (HIFU) lithotripsy with cavitation micro-bubbles and investigated the cavitation detection method to optimize the HIFU intensity.[5] The sonoporation generated by the cavitation bubble collapse can induce transient pores in cell membranes.[6] Ohl *et al.* indicated that the sonoporation caused by the non-spherical bubble collapse near the boundary is responsible for cell detachment.[7] The sonoporation, as the main mechanism of ultrasonic gene transfection and drug delivery, has received increasing attention in biomedicine recently.[8–10] Investigating the cavitation bubble collapse is crucial for improving the applications of sonoporation. Kornfeld and Suvarov first conducted the theoretical and experimental studies on the destructive effect of cavitation bubble collapse in 1944.[11] Benjamin and Ellis investigated the physical mechanism of cavitation bubble collapse near a rigid wall in 1966.[12] Although the dynamic process of cavitation bubble collapse can be observed in experiments via the high-speed photography,[13] the collapse details still cannot be captured accurately. Meanwhile, Plesset and Chapman first conducted a numerical analysis on the collapse of an initially spherical bubble near a solid boundary in 1971.[14] However, the involved mechanism is complicated that makes it difficult to establish a complete analytic theory for cavitation bubble collapse.

The lattice Boltzmann method (LBM) is a mesoscopic computational fluid dynamics (CFD) method. Unlike the traditional CFD methods, which solve the conservation equations of macroscopic properties numerically, the LBM treats the fluid as a discrete system consisting of massive fictive particles, and such particles perform consecutive migration and collision processes over a discrete lattice mesh. The LBM uses a local distribution function governed by the lattice Boltzmann equation (LBE) to represent the distributions of particles at mesh nodes.[15] Benefiting from its particulate nature and local dynamics, the LBM can reveal the physical nature of fluid flow with relatively simple computing procedure, which makes it a feasible approach for describing the cavitation bubble collapse. The Shan–Chen model is a widely used LBM model for the liquid–vapor flow.[16] Considering that the interaction between bubble and cell is a key topic for applications of cavitation bubble collapse in bio-medicine, a multiple-relaxation-time Shan–Chen (MRT-SC) model based on the D2Q9 square lattice is presented in this work to investigate the bubble dynamics near a curved cell wall.

Fixing the lattice time step dt and spatial step dl to 1 for simplicity, the discrete velocity is

$$\boldsymbol{e}_\alpha = \begin{pmatrix} 0 & 1 & 0 & -1 & 0 & 1 & -1 & -1 & 1 \\ 0 & 0 & 1 & 0 & -1 & 1 & 1 & -1 & -1 \end{pmatrix}, \quad (1)$$

*Supported by the National Natural Science Foundation of China under Grant Nos 11674173, 81627802, 11474161, 11374155 and 11474001, and the Qing Lan Project.

**Corresponding author. Email: dzhang@nju.edu.cn

© 2017 Chinese Physical Society and IOP Publishing Ltd

where the subscript $\alpha = 0, 1, \ldots, 8$. The equilibrium distribution function is

$$f_\alpha^{\rm eq} = \rho w(|\boldsymbol{e}_\alpha|^2)\Big[1 + \frac{\boldsymbol{e}_\alpha \cdot \boldsymbol{u}}{c_{\rm s}^2} + \frac{(\boldsymbol{e}_\alpha \cdot \boldsymbol{u})^2}{2c_{\rm s}^4} - \frac{\boldsymbol{u}^2}{2c_{\rm s}^2}\Big], \quad (2)$$

where $c_{\rm s} = \sqrt{1/3}$ is the lattice speed of sound, $w(|\boldsymbol{e}_\alpha|^2)$ is a coefficient relevant to $|\boldsymbol{e}_\alpha|^2$, $w(0) = 4/9$, $w(1) = 1/9$ and $w(2) = 1/36$, ρ and $\boldsymbol{u}$ are the macroscopic density and flow velocity, respectively. The governing equation is[17]

$$\begin{aligned} & f_\alpha(\boldsymbol{x} + \boldsymbol{e}_\alpha dt, t + dt) \\ &= f_\alpha(\boldsymbol{x}, t) - \sum_\beta \bar{\Lambda}_{\alpha\beta}[f_\beta(\boldsymbol{x}, t) - f_\beta^{\rm eq}(\boldsymbol{x}, t)] \\ &\quad + \Big[s_\alpha(\boldsymbol{x}, t) - \frac{1}{2}\sum_\beta \bar{\Lambda}_{\alpha\beta} s_\beta(\boldsymbol{x}, t)\Big], \end{aligned} \quad (3)$$

where f_α is the local distribution function, s_α is the discrete force term, and $\bar{\Lambda}$ is the so-called collision matrix,

$$\bar{\Lambda} = \boldsymbol{M}^{-1} \cdot \Lambda \cdot \boldsymbol{M}, \quad (4)$$

with $\boldsymbol{M}$ being an orthogonal transformation matrix between the discrete velocity space and the moment space,

$$\boldsymbol{M} = \begin{pmatrix} 1 & 1 & 1 & 1 & 1 & 1 & 1 & 1 & 1 \\ -4 & -1 & -1 & -1 & -1 & 2 & 2 & 2 & 2 \\ 4 & -2 & -2 & -2 & -2 & 1 & 1 & 1 & 1 \\ 0 & 1 & 0 & -1 & 0 & 1 & -1 & -1 & 1 \\ 0 & -2 & 0 & 2 & 0 & 1 & -1 & -1 & 1 \\ 0 & 0 & 1 & 0 & -1 & 1 & 1 & -1 & -1 \\ 0 & 0 & -2 & 0 & 2 & 1 & 1 & -1 & -1 \\ 0 & 1 & -1 & 1 & -1 & 0 & 0 & 0 & 0 \\ 0 & 0 & 0 & 0 & 0 & 1 & -1 & 1 & -1 \end{pmatrix}, \quad (5)$$

and Λ being a diagonal matrix whose diagonal elements are adjustable relaxation times,

$$\Lambda = \mathrm{diag}\left(\tau_\rho^{-1} \quad \tau_e^{-1} \quad \tau_\varsigma^{-1} \quad \tau_j^{-1} \quad \tau_q^{-1} \quad \tau_j^{-1} \quad \tau_q^{-1} \quad \tau_\nu^{-1} \quad \tau_\nu^{-1}\right), \quad (6)$$

where $\tau_\rho = \tau_j = 1$ and $\tau_e = \tau_\varsigma = \tau_q = 0.909$ are fixed, while τ_ν will be determined in the following. Denote $\boldsymbol{s} = (s_0 \ s_1 \ldots \ s_8)^{\rm T}$ as the force term in the discrete velocity space. Generally $\boldsymbol{s}$ is obtained by designing it as $\boldsymbol{S}$ in the moment space and projecting $\boldsymbol{S}$ back to the discrete velocity space as

$$\boldsymbol{s} = \boldsymbol{M}^{-1} \cdot \boldsymbol{S}. \quad (7)$$

Based on the framework of the MRT model, a modified scheme of $\boldsymbol{S}$ was utilized in this work,[18]

$$\boldsymbol{S} = \begin{bmatrix} 0 \\ 6(u_x F_x + u_y F_y) - \frac{0.75\varepsilon|\boldsymbol{F}|^2}{G\psi^2(\tau_e - 0.5)} \\ -6(u_x F_x + u_y F_y) + \frac{0.75\varepsilon|\boldsymbol{F}|^2}{G\psi^2(\tau_\varepsilon - 0.5)} \\ F_x \\ -F_x \\ F_y \\ -F_y \\ 2(u_x F_x - u_y F_y) \\ u_x F_y + u_y F_x \end{bmatrix}, \quad (8)$$

where $\boldsymbol{F}$ is the interaction force between particles, u_x and u_y are the components of $\boldsymbol{u}$, F_x and F_y are components of $\boldsymbol{F}$, and ε is an adjustable parameter for improving the consistency between the model and the thermodynamic theory. If considering only the interaction between the nearest-neighbor particles, $\boldsymbol{F}$ can be written as[19]

$$\boldsymbol{F}(\boldsymbol{x}, t) = -G\psi(\boldsymbol{x}, t)\sum_{\alpha=1}^{8} \omega(|\boldsymbol{e}_\alpha|^2)\psi(\boldsymbol{x} + \boldsymbol{e}_\alpha, t)\boldsymbol{e}_\alpha, \quad (9)$$

where $G = -1$ is the coefficient of interaction strength, $\omega(|\boldsymbol{e}_\alpha|^2)$ is a coefficient related to $|\boldsymbol{e}_\alpha|^2$, $\omega(1) = 1/3$ and $\omega(2) = 1/12$, and $\psi(\boldsymbol{x}, t)$ is the local effective mass as a function of ρ,[20]

$$\psi(\rho) = \sqrt{\frac{2(p_{\rm EOS} - \rho c_{\rm s}^2)}{G}}, \quad (10)$$

where $p_{\rm EOS}$ is the pressure given by the equation of state (EOS). Note that G is only required to ensure a positive term inside the square root, and its value is insignificant for $\boldsymbol{F}$ due to the square operation in Eq. (9). Equation (10) makes it possible to adopt different kinds of EOSs in the model. In this work, the Carnahan–Starling (CS) EOS[21] is adopted,

$$p_{\rm EOS} = \rho RT\frac{1 + (b\rho/4) + (b\rho/4)^2 - (b\rho/4)^3}{(1 - b\rho/4)^3} - a\rho^2, \quad (11)$$

where R is the gas constant, $a = 0.4963(RT_{\rm c})^2/p_{\rm c}$, $b = 0.1873RT_{\rm c}/p_{\rm c}$, $T_{\rm c}$ and $p_{\rm c}$ are the critical temperature and pressure, respectively. The previous work[22] indicates that decreasing a could decline the spurious currents near the phase interface and could enhance the numerical stability at large liquid–vapor density ratio. In this work, $R = 1$, $a = 0.5$ and $b = 4$ were adopted, thereby giving $T_{\rm c} = 0.0472$. Combining with the above components, Eq. (3) can be solved consequently to determine f_α, thereby defining ρ and $\boldsymbol{u}$ as

$$\rho = \sum_a f_a, \rho\boldsymbol{u} = \sum_a f_a \boldsymbol{e}_a + \boldsymbol{F}dt/2. \quad (12)$$

The cavitation phenomena is essentially a phase transition from liquid to vapor. A square region (100×100 lattices) is filled with pure liquid ($T = 0.8T_{\rm c}$ and $\rho_0 = 0.2$). To induce the phase transition, an extremely small density perturbation of $10^{-8}\rho_0$ is added on the horizontal symmetric line of the square region at the initial time ($t = 0$). The adjustable coefficient $\varepsilon = 5$ and relaxation time $\tau_\nu = 0.8$ are adopted. Moreover, the periodic boundary condition is implemented at the four boundaries of the square region to simulate the environment. By using the MRT-SC model, Fig. 1 illustrates the density variations at two different

locations in the square region. The blue curve represents the location of $(50, 50)$, while the red one represents the location of $(50, 0)$. The two-dimensional density distributions over the square region at certain time steps are also attached in Fig. 1. It can be observed that at the initial stage, the densities at both locations are almost the same, the density distribution of the square region is constant, and there are no different phases. After about 600 time steps, the density at the location of $(50, 0)$ rises rapidly and tends to be constant after a tempestuous oscillation, while the density at the location of $(50, 50)$ declines rapidly and tends to be constant after a slight fluctuation. During this stage, there appears distinct density variation throughout the square region, the liquid and vapor phases can be distinguished. Eventually, a steady liquid–vapor coexistent system is formed, and the phase interface with finite thickness is flat due to the initial linear density perturbation. Furthermore, the final densities at the locations of $(50, 50)$ and $(50, 0)$ are the coexistence vapor density $\rho_{\rm vco}$ and liquid density $\rho_{\rm lco}$, respectively, at $T = 0.8T_{\rm c}$. Similarly, $\rho_{\rm vco}$ and $\rho_{\rm lco}$ at different temperatures ($< T_{\rm c}$) can be obtained.

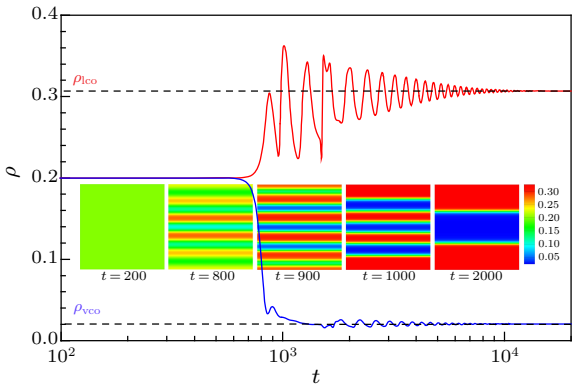

Fig. 1. Density variation as a function of time.

By using the MRT-SC model, Fig. 2 shows the coexistence densities as a function of temperature at different values of ε and τ_ν, respectively. The non-monotonic curve is the theoretical coexistence curve obtained via thermodynamic theory, and its left and right branches correspond to the vapor and liquid phases, respectively. The coexistence curve reveals that the coexistence densities $\rho_{\rm lco}$ and $\rho_{\rm vco}$ at $T_{\rm c}$ are equal, and their ratio $\rho_{\rm lco}/\rho_{\rm vco}$ raises tempestuously with the decrease of T. It can be observed from Fig. 2(a) that $\rho_{\rm lco}$ and $\rho_{\rm vco}$ obtained by the MRT-SC model increasingly overlap with the theoretical coexistence curve with T approaching $T_{\rm c}$. However, various degrees of deviations emerge and become more remarkable with the decrease of T at different values of ε. It is worth noting that the case of a lower temperature (i.e., higher $\rho_{\rm lco}/\rho_{\rm vco}$) requires a larger ε, otherwise the MRT-SC model could encounter the numerical instability. In addition, it can be observed in Fig. 2(b) that the value of τ_ν has slight influences on the coexistence densities obtained by the MRT-SC model. On the basis of the above results, the MRT-SC model becomes more consistent with the thermodynamic theory with the temperature approaching $T_{\rm c}$. To minimize the thermodynamic inconsistency over a wide temperature range, $\varepsilon = 5.53$ and $\tau_\nu = 1.15$ are adopted.

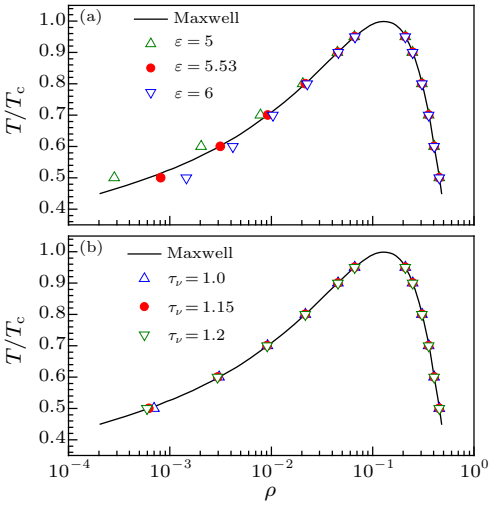

Fig. 2. Coexistence densities as a function of T at different values of (a) ε and (b) τ_ν.

Theoretically, the phenomenon that a vapor bubble remains steady in liquid can be explained by the Young–Laplace equation

$$\Delta p_{\rm L} = p_{\rm l} - p_{\rm v} = -\frac{\sigma}{R_{\rm s}}, \tag{13}$$

where $\Delta p_{\rm L}$ is the Laplace pressure, $p_{\rm l}$ is the external liquid pressure, $p_{\rm v}$ is the internal vapor pressure, σ is the surface tension strength, and $R_{\rm s}$ is the radius of the steady bubble. Equation (13) indicates that $\Delta p_{\rm L}$ is proportional to $1/R_{\rm s}$, which could be used to validate the MRT-SC model. To obtain a vapor bubble in liquid, Huang *et al.* proposed an initialization approach for density,[23]

$$\rho(x, y) = \frac{\rho_{\rm l0} + \rho_{\rm v0}}{2} - \frac{\rho_{\rm l0} - \rho_{\rm v0}}{2} \cdot \tanh\left[\frac{2(\sqrt{(x - x_0)^2 + (y - y_0)^2} - R_0)}{W_0}\right], \tag{14}$$

where (x_0, y_0) is the initial position of the bubble center, R_0 is the initial radius of the bubble, W_0 is the initial thickness of the phase interface, $\rho_{\rm l0}$ and $\rho_{\rm v0}$ are the initial densities of liquid and vapor, respectively. The density of a square region (200×200 lattices) is initialized by Eq. (14) with $x_0 = 100$, $y_0 = 100$ and $W_0 = 5$. Here $\rho_{\rm l0}$ and $\rho_{\rm v0}$ are set to the coexistence densities $\rho_{\rm lco}$ and $\rho_{\rm vco}$ to reduce the consumed time for

the initial bubble achieving stability. Assigning that the density of the phase interface is $(\rho_{l0}+\rho_{v0})/2$, Fig. 4 shows the positive pressure difference Δp ($p_l < p_v$) as a function of $1/R_s$ at different temperatures. Considering that Δp_L tends to be zero with R_s approaching to infinity according to Eq. (12), a zero-axial linear fit curve of the results is plotted in Fig. 3, and its slope represents the surface tension strength σ. It can be observed that Δp is almost perfectly proportional to $1/R_s$, and the slope of fit curve declines with the increase of temperature. This is consistent with the thermodynamic theory.[24]

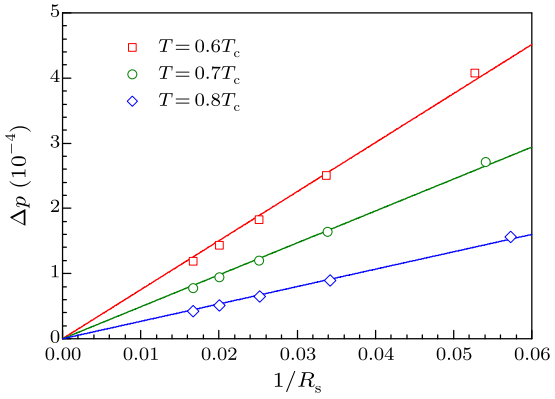

Fig. 3. The value of Δp as a function of $1/R_s$ at different temperatures.

Using the MRT-SC model, the evolution of bubble near a solid circular wall can be investigated qualitatively. Equation (14) is used to obtain an initial bubble with $R_0 = 100$, $W_0 = 5$, $\rho_{l0} = 0.49$ and $\rho_{v0} = 0.0002$, which gives $\Delta p = 0.0204$ at $T = 0.8T_c$ ($p_l < p_v$, the extra pressure cussed by the phase interface is not included). A dimensionless coefficient λ is assigned to represent the initial distance between the bubble and wall,

$$\lambda = (D - R_w)/R_0, \tag{15}$$

where R_w is the curvature radius of the wall, D is the initial distance between the curvature centers of the bubble and wall, $R_w = 10R_0$ and $\lambda = 1.5$ are adopted in this work. The non-equilibrium extrapolation boundary conditions are used at the left, right and upper boundaries to simulate the environment, while the Bouzidi–Firdaouss–Lallemand (BFL) boundary condition[25] is used at the wall. Assigning that the strict liquid–vapor interface locates at the positions with the density of $(\rho_l + \rho_v)/2$, Fig. 4 exhibits the deformation of the bubble with time. Note that the calculated results are traditionally in lattice units for convenience. To obtain the corresponding physical information, the dimensional analysis was adopted for unit conversion between the lattice units and physical units (SI). Consequently, the initial radius of bubble ($R_0 = 100$) is about 95 nm, and the outside-in time steps in Fig. 4 are 0 ns, 0.0713 ns, 0.1425 ns, 0.2138 ns, 0.2495 ns, 0.2637 ns, 0.2780 ns and 0.2922 ns, respectively. The dark region represents the solid circular wall. It can be observed that, at the initial stage, the bubble shrinks under the pressure difference, immediately following a differential deformation that the longitudinal shrinkage rate is lower than the transverse one. Subsequently, an inward concave emerges on the top of the bubble, and is exacerbated dramatically. Finally, the concave rushes to the internal bottom of the bubble, thereby collapsing the bubble. An explanation of the deformation process of the bubble is that the presence of the solid circular wall breaks the symmetry of the external pressure distribution around the bubble, and the pressure above the bubble is much higher than the pressure under the bubble. Thus the top interface shrinks faster than the bottom interface, which results in a concave. Meanwhile, the location of the bubble moves down. At the final stage of deformation, the top interface strikes the bottom interface violently under a local pressure gradient, and collapses the bubble with a high-speed jet. It is worth noting that the downward jet has a columnar shape and could impact the wall with damage.

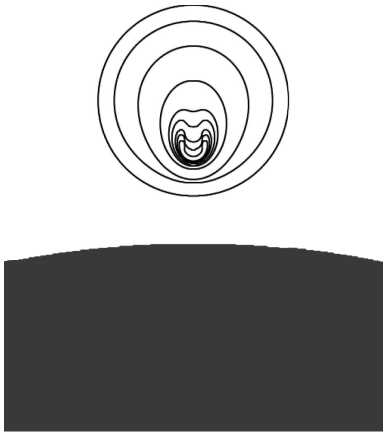

Fig. 4. Deformation of bubble with time.

To describe the deformation of the bubble, the collapsing time is assigned as the time step when the bubble collapses, and the jet speed is assigned as the maximal speed around the collapsing region at the collapsing time. The initial pressure difference and bubble-wall distance are two key factors affecting the deformation of the bubble. Figure 5 shows the collapsing time and jet speed as functions of Δp and λ. It can be observed in Fig. 5(a) that, with the increase of Δp, the collapsing time reduces and the jet speed rises. It is easy to understand that a higher Δp can intensify the deformation of the bubble. However, the influence of λ on the deformation of the bubble is relatively complicated. It can be observed in Fig. 5(b) that, with the increase of λ, the collapsing time still reduces while the jet speed rises first and then de-

clines. It can be explained such that the deformation and the collapse-generated jet are suppressed by the wall when λ is relatively small, and such a suppression recedes with the increasing λ. However, the shrinkage under the pressure difference contributes more than the presence of the wall to the deformation of bubble when λ is relatively large, thus the local pressure gradient around the collapsing region decreases, thereby reducing the jet speed.

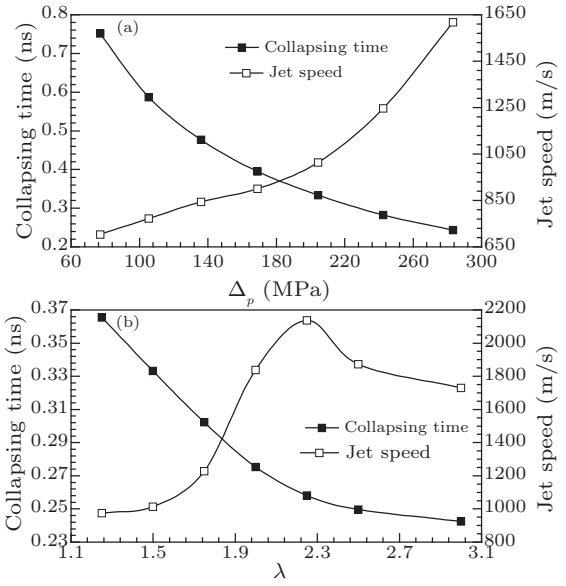

Fig. 5. Collapsing time and jet speed as functions of (a) Δp and (b) λ.

In conclusion, the MRT-SC model based on the D2Q9 square lattice has been presented to describe the liquid–vapor flow. By using this model, the cavitation phenomena induced by density perturbation are simulated to obtain the coexistence densities at certain temperature and to demonstrate the Young–Laplace equation. Then, the cavitation bubble collapse near a curved wall is simulated. Moreover, the influences of initial pressure difference and bubble-wall distance on the cavitation bubble collapse are investigated. The results indicate that the MRT-SC model could be consistent with the thermodynamic theory by adopting appropriate parameters, and the cavitation bubble collapse near a curved wall generates a high-speed jet that could damage the wall.

References

[1] Lauterborn W and Bolle H 1975 *J. Fluid Mech.* **72** 391
[2] Miller M W, Miller D L and Brayman A A 1996 *Ultrasound Med. Biol.* **22** 1131
[3] Carstensen E L, Gracewski S and Dalecki D 2000 *Ultrasound Med. Biol.* **26** 1377
[4] Salgaonkar V A, Datta S, Holland C K and Mast T D 2009 *J. Acoust. Soc. Am.* **126** 3071
[5] Yoshizawa S, Ikeda T, Ito A, Ota R, Takagi S and Matsumoto Y 2009 *Med. Biol. Eng. Comput.* **47** 851
[6] Wu J, Pepe J and Rincón M 2006 *Ultrasonics* **44** e21
[7] Ohl C D, Arora M and Ikink R 2006 *Biophys. J.* **91** 4285
[8] Ward M, Wu J and Chiu J F 1999 *J. Acoust. Soc. Am.* **105** 2951
[9] Hauff P, Seemann S, Reszka R, Schultze-Mosgau M, Reinhardt M, Buzasi T, Plath T, Rosewicz S and Schirner M 2005 *Radiology* **236** 572
[10] Wu J and Nyborg W L 2008 *Adv. Drug. Deliver. Rev.* **60** 1103
[11] Kornfeld M and Suvarov L 1944 *J. Appl. Phys.* **15** 495
[12] Benjamin T B and Ellis A T 1966 *Philos. Trans. R. Soc. London. Ser.* A **260** 221
[13] Philipp A and Lauterborn W 1998 *J. Fluid Mech.* **361** 75
[14] Plesset M S and Chapman R B 1971 *J. Fluid Mech.* **47** 283
[15] Shan X and He X 1998 *Phys. Rev. Lett.* **80** 65
[16] Shan X and Chen H 1993 *Phys. Rev.* E **47** 1815
[17] Michael E, McCracken E and Abraham J 2005 *Phys. Rev.* E **71** 036701
[18] Li Q, Luo K H and Li X J 2013 *Phys. Rev.* E **87** 053301
[19] Shan X 2006 *Phys. Rev.* E **73** 047701
[20] He X and Doolen G D 2002 *J. Stat. Phys.* **107** 309
[21] Yuan P and Schaefer L 2006 *Phys. Fluids* **18** 042101
[22] Wei Y K and Qian Y H 2012 *Chin. Phys. Lett.* **29** 064705
[23] Huang H B, Krafczyk M and Lu X Y 2011 *Phys. Rev.* E **84** 046710
[24] Gittens G J 1969 *J. Colloid Interface Sci.* **30** 406
[25] Bouzidi M, Firdaouss M and Lallemand P 2001 *Phys. Fluids* **13** 3452